



Cite this: *Chem. Sci.*, 2022, 13, 754

All publication charges for this article have been paid for by the Royal Society of Chemistry

# Single-atom cobalt-hydroxyl modification of polymeric carbon nitride for highly enhanced photocatalytic water oxidation: ball milling increased single atom loading†

Fei Yu, Tingting Huo, Quanhua Deng, Guoan Wang, Yuguo Xia,  Haiping Li \* and Wanguo Hou

Expediting the oxygen evolution reaction (OER) is the key to achieving efficient photocatalytic overall water splitting. Herein, single-atom Co–OH modified polymeric carbon nitride (Co-PCN) was synthesized with single-atom loading increased by ~37 times with the assistance of ball milling that formed ultrathin nanosheets. The single-atom Co–N<sub>4</sub>OH structure was confirmed experimentally and theoretically and was verified to enhance optical absorption and charge separation and work as the active site for the OER. Co-PCN exhibits the highest OER rate of 37.3  $\mu\text{mol h}^{-1}$  under visible light irradiation, ~28-fold higher than that of common PCN/CoO<sub>x</sub>, with the highest apparent quantum yields reaching 4.69, 2.06, and 0.46% at 400, 420, and 500 nm, respectively, and is among the best OER photocatalysts reported so far. This work provides an effective way to synthesize efficient OER photocatalysts.

Received 24th November 2021

Accepted 14th December 2021

DOI: 10.1039/d1sc06555f

rsc.li/chemical-science

Massive fuel energy consumption induced environmental and ecological problems, especially the greenhouse effect, and the resultant extreme climates and rise in sea level are threatening human life.<sup>1</sup> As a potential substitution for fuel energy, hydrogen energy conversion from solar energy *via* photocatalytic water splitting attracts great attention from scientists.<sup>2–5</sup> However, the photocatalytic hydrogen evolution efficiency from overall water splitting is still restricted by the sluggish oxygen evolution reaction (OER) that involves energy absorption, four-electron transfer, breakage of O–H bonds, and formation of O–O bonds,<sup>6,7</sup> and thus efficient OER photocatalysts become the key to achieving efficient overall water splitting. Though numerous hydrogen evolution photocatalysts have been reported, research on OER photocatalysts is mainly around a few semiconductors including BiVO<sub>4</sub>, WO<sub>3</sub>, Ag<sub>3</sub>PO<sub>4</sub>,  $\alpha$ -Fe<sub>2</sub>O<sub>3</sub>, *etc.*<sup>8–11</sup> and their activity is not high enough yet for practical applications. Therefore, exploring high-efficiency OER photocatalysts is still necessary.

Polymeric carbon nitride (PCN) was first reported in 2009 (ref. 12) as a photocatalyst with a layered melon-type

orthorhombic structure,<sup>13</sup> and thereafter quickly became a “star” photocatalyst thanks to its advantages of being visible-light responsive and metal-free, non-toxic, and low cost, and its relatively high chemical stability.<sup>14</sup> Because of several self-deficiencies including fast photogenerated charge recombination and a narrow optical absorption spectrum, PCN exhibits relatively low photocatalytic activity.<sup>15</sup> Then, a series of strategies were put forward successively to enhance the photoactivity of PCN, such as enhancement of crystallinity,<sup>16</sup> morphological control,<sup>17</sup> structural modification<sup>18</sup> (including extensively researched single atom modification in recent years<sup>19,20</sup>), exfoliation,<sup>21</sup> construction of hetero-(homo-)junctions,<sup>22</sup> and loading of noble metals.<sup>23</sup> Though photocatalytic water splitting on PCN was extensively researched in the past, the research was mainly around the hydrogen evolution half-reaction used for exploring properties and the catalytic mechanism of photocatalysts, and little research was focused on the industrially useable overall water splitting process owing to the sluggish OER.<sup>15</sup> Therefore, enhancing the photocatalytic OER activity of PCN becomes the key to practical applications.

To increase OER rates of PCN, several kinds of methods were proposed, such as rational design of compound cocatalysts (*e.g.*, CoO<sub>x</sub>, IrO<sub>2</sub>, CoP, CoPi, RhO<sub>x</sub>, RuO<sub>x</sub>, PtO<sub>x</sub>, MnO<sub>x</sub>, Co(OH)<sub>2</sub>, Ni(OH)<sub>2</sub>, and CoAl<sub>2</sub>O<sub>4</sub> (ref. 24–30)), modification of carbon dots and carbon rings,<sup>31,32</sup> fabrication of special architectures of PCN (*e.g.*, PCN quantum dot stacked nanowires<sup>33</sup>), and single-atom (*e.g.*, B, Co, and Mn<sup>34–36</sup>) modification. For instance, Zhao and coauthors prepared B and N-vacancy comodified PCN that exhibits the highest OER rate of ~28  $\mu\text{mol h}^{-1}$  (ref. 36) and

National Engineering Research Center for Colloidal Materials, School of Chemistry and Chemical Engineering, Shandong University, Jinan, Shandong, 250100, China. E-mail: hpli@sdu.edu.cn

† Electronic supplementary information (ESI) available: Synthesis of samples, details of characterization, partial SEM and TEM images, XANES and EXAFS spectra, XPS spectra, photocatalytic OER data, XRD patterns, XANES and EXAFS fitting data, VB-XPS and FT-IR spectra, nitrogen sorption data, zeta potential and Mott-Schottky plots, DFT calculation results of energy bands and DOS, and elemental analysis data (PDF). See DOI: 10.1039/d1sc06555f

recently their group further used these B doped PCN ultrathin nanosheets to fabricate a Z-scheme heterojunction for overall water splitting with a solar-to-hydrogen efficiency reaching  $\sim 1.2\%$ .<sup>37</sup> Comparatively, PCN loaded with compound cocatalysts can only enhance OER activity to a limited degree and there are finite methods for carbon modification and special architecture fabrication. Single-atom modification shows a bright prospect, on account of metal atoms capable of being inserted into the framework of PCN and effectively increasing the OER activity. However, reported single metal atom modification routes are all based on direct ion adsorption on PCN or calcination of mixtures of metal salts and PCN feedstocks.<sup>34,35,38</sup> New routes need to be explored to increase effective loading of single atoms in PCN. Besides, the metal-OH structure is considered efficient for the OER,<sup>30,39,40</sup> and a single metal atom-OH structure has never been reported for modification of PCN, though Mn-OH was thought to play a key role in the OER process.<sup>34</sup>

Ball milling is an extensively used versatile and scalable way for preparation of heterogeneous catalysts and even single-atom

catalysts,<sup>41,42</sup> but was rarely used in synthesis of PCN-based single-atom photocatalysts. In this work, we synthesized single-atom Co-OH modified PCN (Co-PCN) with the single-atom content in PCN highly increased with the assistance of ball milling. The simple synthetic route is shown in Fig. 1a. PCN was ball-milled to obtain BM-PCN that then adsorbed  $\text{Co}^{2+}$  till saturation to form BM-PCN/Co which was calcined to obtain BM-PCN/Co-c (Co-PCN). For comparison, PCN was directly used to adsorb  $\text{Co}^{2+}$  till saturation to form PCN/Co which was calcined to obtain PCN/Co-c. PCN mainly comprises large blocks with the size of several micrometers (Fig. S1†), while BM-PCN contains massive irregular particles with the size reduced to several hundreds of nanometers (Fig. S2†), indicative of high efficacy of ball milling. BM-PCN/Co-c exhibits a similar morphology as BM-PCN (Fig. 1b and S3†) and PCN/Co-c exhibits a similar morphology to PCN (Fig. S4†), but the surface area and mesopore volume of BM-PCN and BM-PCN/Co-c are not higher than those of PCN and PCN/Co-c (Fig. S5†), manifesting that ball-milling and subsequent calcination did not form massive

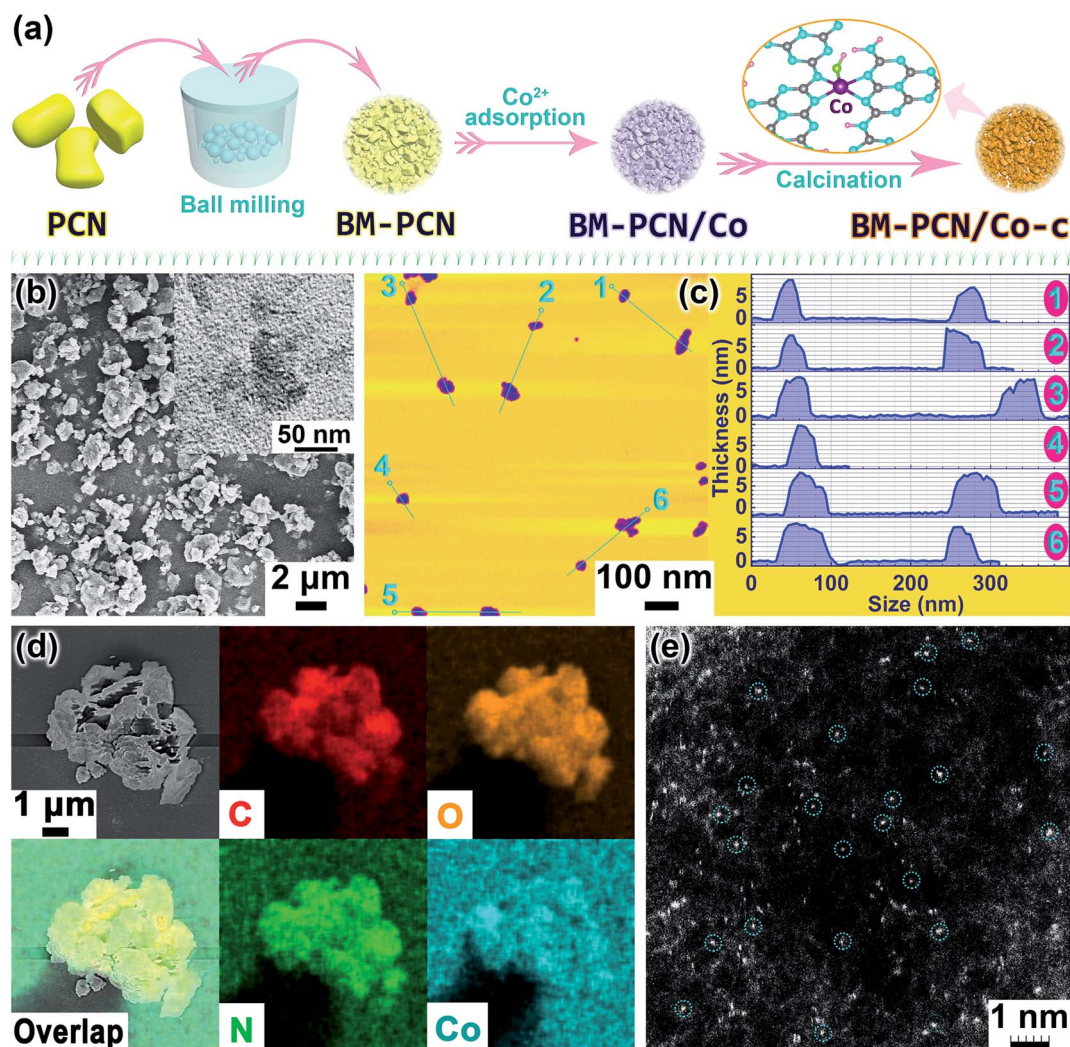


Fig. 1 (a) Schematic illustration for synthesis of single-atom  $\text{Co}^{\text{II}}$ -OH modified PCN (BM-PCN/Co-c); and (b) SEM, (inset in b) TEM, (c) AFM, (d) EDS elemental mapping, and (e) HAADF-STEM images of BM-PCN/Co-c.



mesopores, which accords well with the particle size variation from several micrometers (before ball milling) to several hundreds of nanometers (after ball milling). However, the Co content in BM-PCN/Co-c, BM-PCN/Co, PCN/Co-c, and PCN/Co was measured to be 0.75, 0.50, 0.02, and  $\sim 0.02$  wt%, respectively, by inductively coupled plasma mass spectrometry (ICP-MS). The  $\sim 37$  times higher Co content in BM-PCN/Co-c than in PCN/Co-c suggests the ball-milling enhanced adsorption of  $\text{Co}^{2+}$  on surfaces of BM-PCN, which should arise mainly from the ball-milling induced increase of surface energy and adsorption sites.<sup>43</sup>

The TEM image shows the existence of small and ultrathin nanosheets in BM-PCN/Co-c (inset in Fig. 1b) which can also be observed in the atomic force microscopy (AFM) image with a thickness of  $\sim 7$ –10 nm and lateral size of  $< 70$  nm (Fig. 1c), and formation of these ultrathin nanosheets results from the ball

milling of PCN.<sup>44</sup> It should be noted that most formed ultrathin nanosheets with high surface energy may stack into compact particles upon ball milling, leading to no increase of the total surface area. Energy dispersive X-ray spectroscopy (EDS) elemental mapping images of BM-PCN/Co-c indicate homogeneous distribution of C, N, O, and Co elements in the sample (Fig. 1d). The high-angle annular dark-field scanning transmission electron microscopy (HAADF-STEM) image of BM-PCN/Co-c shows massive white spots (marked by circles) with a mean size of  $< 1$  Å dispersed in the sample (Fig. 1e and S6†), which should correspond to single-atom Co.

To further verify the single-atom Co structure in BM-PCN/Co-c, Co K-edge X-ray absorption near-edge structure spectroscopy (XANES) and extended X-ray absorption fine structure (EXAFS) analysis were performed. As shown in Fig. 2a, the absorption-edge position of BM-PCN/Co-c is quite close to that of CoO and

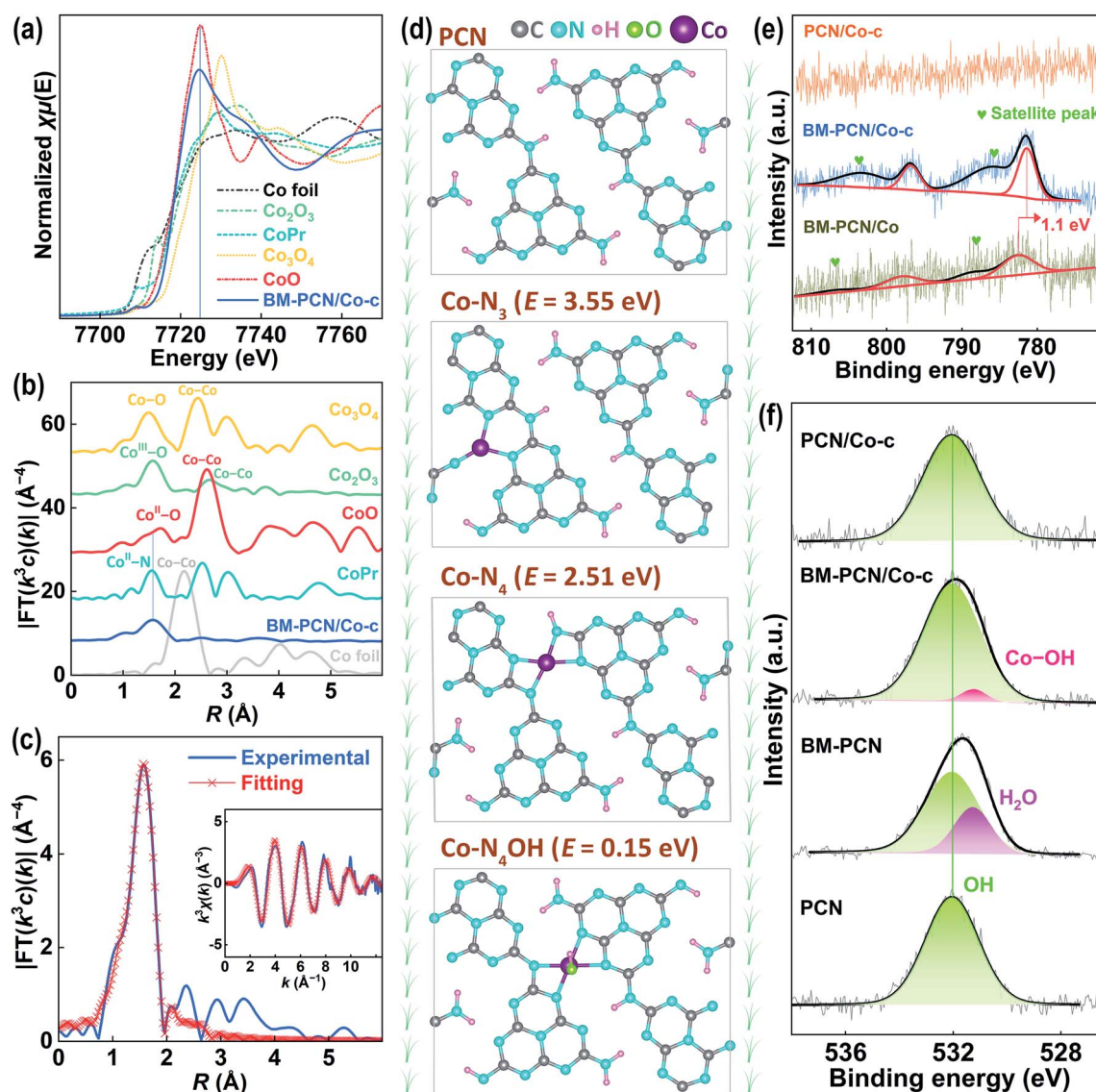


Fig. 2 (a) Co K-edge XANES and (b) EXAFS spectra of Co foil, Co porphyrin (CoPr),  $\text{Co}_3\text{O}_4$ ,  $\text{Co}_2\text{O}_3$ , and BM-PCN/Co-c; EXAFS (c) R space-fitting and (inset in c) K space-fitting curves of BM-PCN/Co-c; (d) optimized structure of PCN and Co-doped PCN with different doping configurations and calculated formation energies (e) of Co doped PCN; and (e) Co 2p and (f) O 1s core-level XPS spectra of samples.



their peak positions are similar and far from those of other reference samples, indicating that the valence of Co in BM-PCN/Co-c is about +2. The bonding structure around Co was determined by Fourier transformed (FT)  $k^3$ -weighted EXAFS analysis. As shown in Fig. 2b, a distinct single Co-ligand peak at  $\sim 1.6$  Å for BM-PCN/Co-c is observed, which prominently differs from the Co-Co coordination peak at  $\sim 2.2$  Å for Co foil and the Co<sup>II</sup>-O coordination peak at  $\sim 1.7$  Å for CoO. The wavelet transform (WT) contour plot of BM-PCN/Co-c shows only one intensity maximum (Fig. S7†), and the Cl 2p core-level XPS spectrum of BM-PCN/Co-c reveals no residue of Cl (Fig. S8†). These further indicate the single-atom dispersion of Co species. Apparently, the Co-ligand peak is almost consistent with the Co<sup>II</sup>-N peak for Co porphyrin, suggesting that the single-atom Co in BM-PCN/Co-c mainly coordinates with N. Least-square EXAFS curve fitting was performed to confirm quantitative structural parameters of Co<sup>II</sup> in BM-PCN/Co-c, as shown in Fig. 2c, S9, and S10 and Table S1.† Simple Co-N single-shell fitting of BM-PCN/Co-c (Fig. S10†) gave a coordination number of  $5.6 \pm 0.4$  (Table S1†), that is, Co<sup>II</sup> coordinates with five atoms. Considering that the PCN monolayer provides four appropriate N coordination sites at most,<sup>45</sup> Co<sup>II</sup> likely coordinates with four N atoms and one OH atom. Thus, we further performed Co-N<sub>4</sub>/Co-O double-shell fitting (Fig. 2c) and the obtained *R*-factor (0.0011) remarkably reduces relative to that from Co-N single-shell fitting (0.0035), indicative of rationality of the proposed Co<sup>II</sup>-N<sub>4</sub>OH structure. Confirmed Co-N and Co-O bond lengths are 2.04 and 2.15 Å, respectively (Table S1†).

To further confirm rationality of the Co-N<sub>4</sub>OH coordination structure, density functional theory (DFT) calculations were conducted. As shown in Fig. 2d, three possible Co<sup>II</sup> coordination structures in the PCN monolayer were explored. The Co-N<sub>4</sub>OH structure without removal of H from PCN exhibits a much lower formation energy ( $\sim 0.15$  eV) than Co-N<sub>4</sub> and Co-N<sub>3</sub> structures with removal of two H atoms from PCN ( $\sim 2.51$  and  $3.55$  eV), demonstrating a high probability of existence of the Co-N<sub>4</sub>OH structure in BM-PCN/Co-c. This structure can also be evidenced by X-ray photoelectron spectroscopy (XPS). As shown in Fig. 2e, the Co 2p core-level XPS spectrum of BM-PCN/Co-c shows two distinct peaks at binding energies of 796.8 and 781.4 eV beside satellite peaks, corresponding to Co 2p<sub>1/2</sub> and 2p<sub>3/2</sub> of Co<sup>II</sup> ions.<sup>46</sup> The spectrum of BM-PCN/Co also shows two Co 2p peaks but at a binding energy  $\sim 1.1$  eV higher, suggesting variation of the Co coordination structure from BM-PCN/Co to BM-PCN/Co-c. PCN/Co-c exhibits no peaks because of its low Co content. Fig. 2f shows O 1s core-level spectra of PCN, BM-PCN, BM-PCN/Co-c, and PCN/Co-c. All the samples exhibit one peak at a binding energy of  $\sim 532.0$  eV, ascribed to surface hydroxyl species,<sup>47</sup> but an additional peak could be obtained for BM-PCN or BM-PCN/Co-c after deconvolution. The peak at a binding energy of  $\sim 531.3$  eV for BM-PCN should be assigned to adsorbed H<sub>2</sub>O at new active adsorption sites generated by ball milling. This peak can also be observed in the spectrum of BM-PCN/Co, but with a  $\sim 0.1$  eV shift to a higher binding energy (Fig. S11†) owing to the influence of adsorbed Co<sup>II</sup> ions. The peak at  $\sim 531.2$  eV for BM-PCN/Co-c should be assigned to Co-OH,<sup>48</sup> given that there is only one O 1s peak for BM-PCN-c

(synthesized by direct calcination of BM-PCN) (Fig. S11†). The calculated Co/O(-Co) molar ratio, based on the XPS data, is  $\sim 1.07$  (Table S2†), close to 1, consistent with the Co-N<sub>4</sub>OH coordination structure.

In C 1s and N 1s core-level XPS spectra, BM-PCN, BM-PCN/Co-c, PCN/Co-c, and BM-PCN/Co exhibit similar peaks to PCN (Fig. S12a-d†), indicative of their similar framework structure which can also be evidenced by their similar N/C molar ratios, 1.53 (Table S3†), but the N-H peak of BM-PCN shifts  $\sim 0.2$  eV to a lower binding energy relative to that of PCN, likely arising from the ball-milling induced destruction of intralayer hydrogen bonds (Fig. S13†). The Co content in BM-PCN/Co, BM-PCN/Co-c, and PCN/Co-c is too low to cause detectable variation of C 1s and N 1s peaks. Similar FT-IR absorption bands of the samples (Fig. S14a and b†) also indicate their basic frame structure, but in enlarged spectra (Fig. S14c†),  $\nu(\text{C-N})$  and  $\nu(\text{C= N})$  absorption bands of BM-PCN shift  $16\text{ cm}^{-1}$  to a higher wavenumber and  $19\text{ cm}^{-1}$  to a lower wavenumber, respectively, relative to those of PCN at  $1242$  and  $1640\text{ cm}^{-1}$ ,<sup>49</sup> likely resulting from the ball-milling induced hydrogen bond destruction, and the shift of these two absorption bands turns smaller for BM-PCN/Co-c, suggesting calcination-induced reforming of the destroyed hydrogen bonds, which is consistent with the XPS results (Fig. S12c†). Besides, BM-PCN exhibits a wider and relatively stronger  $\nu(\text{N-H})/\nu(\text{O-H})$  absorption band than PCN (Fig. S14a†), probably owing to the hydrogen bond destruction and new adsorbed H<sub>2</sub>O, while this absorption band for BM-PCN/Co-c becomes much weaker, suggesting hydrogen bond reforming and loss of new adsorbed H<sub>2</sub>O (Fig. 2f). Zeta potentials of the samples dispersed in water reflect variation of surface adsorbed hydroxyl species. As shown in Fig. S15a,† all the samples exhibit negative zeta potentials because of dissociation of surface hydroxyl species. The zeta potentials, following the order PCN ( $-24\text{ mV}$ ) > BM-PCN ( $-41\text{ mV}$ ) < BM-PCN/Co-c ( $-30\text{ mV}$ )  $\approx$  PCN/Co-c ( $-28\text{ mV}$ ), suggest the ball milling-induced increase of surface hydroxyls in BM-PCN and calcination-induced decrease in BM-PCN/Co-c, consistent with the FT-IR results.

Solid-state <sup>13</sup>C magic-angle-spinning nuclear magnetic resonance (NMR) spectra of PCN, BM-PCN, BM-PCN/Co-c, and PCN/Co-c show two similar peaks at chemical shifts of  $\sim 164$  and  $156\text{ ppm}$  (Fig. S15b†), ascribed to C-NH<sub>x</sub> and N=C-N, respectively,<sup>50</sup> indicating their similar molecular framework, but in enlarged spectra, BM-PCN exhibits  $\sim 0.3^\circ$  movement of the N=C-N peak to a lower chemical shift compared with PCN, because of the ball-milling induced hydrogen bond destruction, and the C-NH<sub>x</sub> peak of BM-PCN/Co-c moves  $\sim 0.2^\circ$  to a lower chemical shift, likely owing to formation of the C-N-Co structure whose peak lies close to the C-NH<sub>x</sub> peak.<sup>51</sup> The XRD patterns of the samples are shown in Fig. S15c.† PCN and PCN/Co-c exhibit typical diffraction peaks of melon-type carbon nitride with a layered orthorhombic structure and peaks at  $13.1^\circ$  and  $27.6^\circ$  correspond to (210) and (002) facets, respectively,<sup>13,52</sup> but BM-PCN reveals remarkably decreased peak intensity and  $\sim 0.2^\circ$  shift of the (002) peak to a lower  $2\theta$  (indicative of the increased interlayer distance) relative to PCN, demonstrating the ball-milling induced hydrogen bond destruction and



substantial decrease of crystallinity. The remarkable decrease of crystallinity and almost no change of the surface area of BM-PCN, compared with those of PCN, further suggest that ball milling may form massive thin nanosheets (Fig. 1c) most of which stack into compact particles (Fig. 1b) owing to their high surface energy. In comparison with BM-PCN, BM-PCN/Co-c exhibits a narrower (002) peak, suggesting enhanced crystallinity owing to the calcination-induced hydrogen bond reforming, consistent with the FT-IR results. On the whole, it is likely the ball-milling induced destruction of hydrogen bonds that contributes largely to the increase of surface energy and new active adsorption centers and thus  $\text{Co}^{2+}$  adsorption on BM-PCN.

Optical absorption capability of samples was investigated by UV-vis diffuse reflectance spectroscopy (DRS). As shown in Fig. 3a, BM-PCN/Co-c, BM-PCN, and PCN/Co-c exhibit considerably higher, lower, and similar optical absorption than/to PCN, respectively. For BM-PCN/Co-c, the optical absorption enhancement at a wavelength of  $<400$  nm may benefit from the electron-rich Co that enhances  $\pi-\pi^*$  transitions in heptazine rings,<sup>53</sup> and the Urbach tail absorption should arise from the Co-OH doping.<sup>54,55</sup> Bandgaps ( $E_g$ ) of PCN, BM-PCN, BM-PCN/Co-c, and PCN/Co-c were roughly confirmed as 2.70, 2.81, 2.56, and 2.73 eV, respectively, *via* the formula  $E_g/\text{eV} = 1240/(\lambda_{\text{ed}}/$

$\text{nm})$ <sup>56</sup> where  $\lambda_{\text{ed}}$  is the absorption edge determined by solid lines in the spectra. The wider  $E_g$  of BM-PCN probably results from the quantum size effect of massive ultrathin crystal nanosheets (Fig. 1c) formed by ball milling, and the narrower  $E_g$  of BM-PCN/Co-c arises from the Co-OH doping that was then verified by DFT calculations. As shown in Fig. S16,<sup>†</sup> the calculated  $E_g$  of BM-PCN/Co-c,  $\sim 1.90$  eV, is much smaller than that of PCN (2.57 eV), in accordance with the experimental results. For PCN, the conduction band (CB) is contributed by C 2p and N 2p orbitals and the valence band (VB) mainly by N 2p orbitals, while for BM-PCN/Co-c, the CB is contributed by Co 3d, C 2p, and N 2p orbitals and the VB mainly by Co 3d and N 2p orbitals (Fig. S16c and d<sup>†</sup>), effectively manifesting that the narrowing of  $E_g$  of BM-PCN/Co-c results from the Co-OH doping. In addition, there are prominent doping levels ( $E_d$ ) in the bandgap of BM-PCN/Co-c, mainly contributed by Co 3d and O 2p orbitals (Fig. S16d<sup>†</sup>), effectively proving the Co-OH doping effect in BM-PCN/Co-c. Similar calculation results have been reported for Pt-OH modified carbon nitride.<sup>57</sup> Given that the experimental Co content (0.75 wt%) is much lower than the theoretical (6.71 wt%), practical doping levels in the bandgap may approach more to the VB. CB edges of the samples ( $E_{\text{CB}}$ ) could be roughly determined by using Mott-Schottky plots (Fig. S17<sup>†</sup>) and their Fermi levels ( $E_f$ ) were subsequently confirmed based on VB-XPS

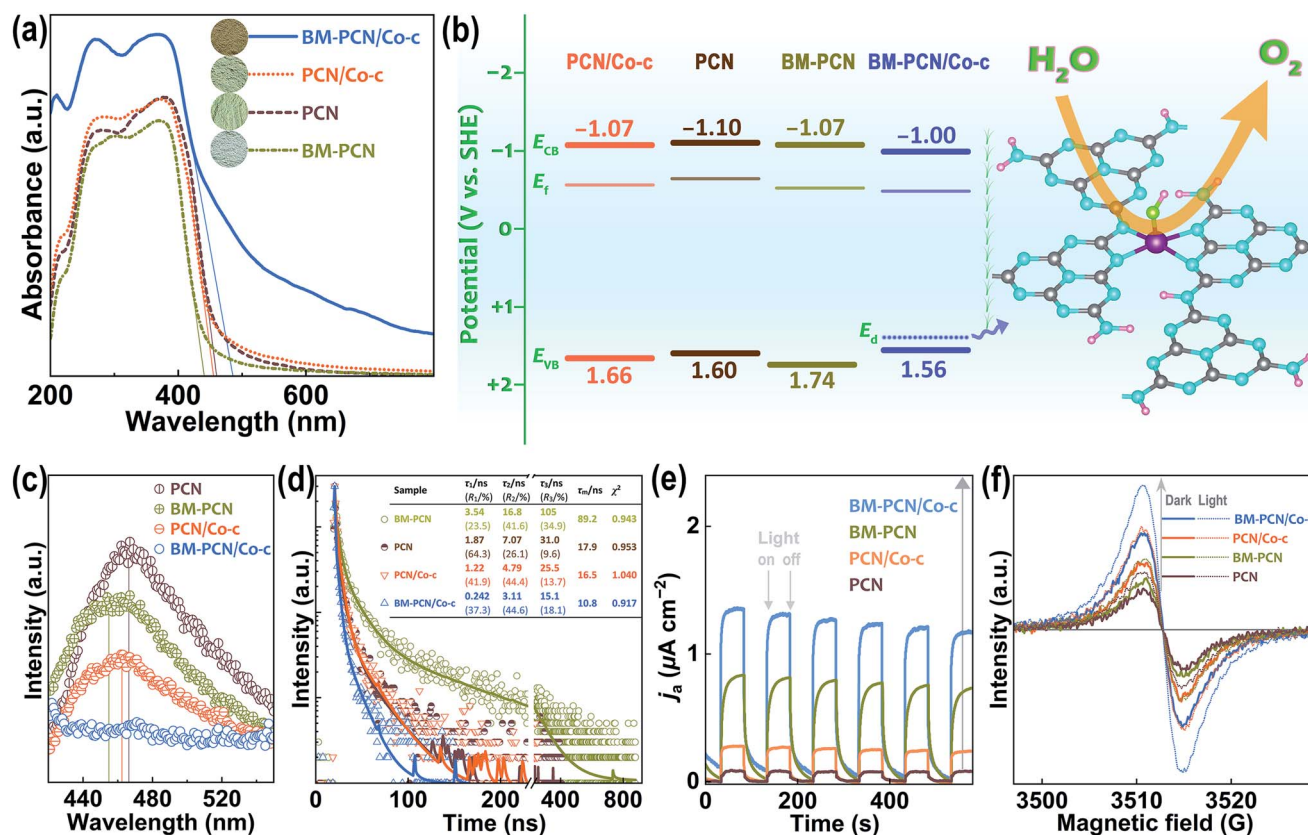


Fig. 3 (a) UV-vis diffuse reflectance spectra of PCN, BM-PCN, BM-PCN/Co-c, and PCN/Co-c; (b) energy band levels of the samples and schematic illustration for water oxidation on BM-PCN/Co-c; (c) photoluminescence spectra, (d) time-resolved fluorescence spectra, and (e) anodic photocurrent ( $J_a$ ) response of the samples; and (f) EPR spectra of the samples in the dark and under visible light irradiation. Data in (d) are the results of fitting decay curves to a tri-exponential model. Dark  $J_a$  in (e) was set as zero for distinct comparison.



spectra (Fig. S18†). Energy band levels of the samples are shown in Fig. 3b, and it seems that ball milling causes a slight downshift of the VB edge ( $E_{VB}$ ) of BM-PCN, favorable for photocatalytic water splitting, but the Co–OH doping causes a slight downshift of  $E_{CB}$  and upshift of  $E_{VB}$  of BM-PCN/Co-c. It is noteworthy that the  $E_d$  close to the VB edge ( $E_{VB}$ ) can capture photogenerated holes<sup>58</sup> and thus the single-atom Co–OH works as the active site for the OER (Fig. 3b).

Spectroscopy and photoelectrochemical tests were conducted to evaluate photogenerated charge separation and transfer performance. As shown in Fig. 3c, photoluminescence (PL) spectra of all the samples show one emission peak, basically corresponding to their bandgap emission. BM-PCN exhibits weaker PL intensity than PCN, revealing a decreased photogenerated charge recombination efficiency, which originates from faster charge transfer from the inside to the surface of ultrathin nanosheets (Fig. S19†) and trapped by surface states.<sup>59</sup> BM-PCN/Co-c exhibits the lowest PL intensity and the PL intensity of PCN/Co-c is lower than that of PCN, which arises from the  $E_d$  capturing photogenerated holes to reduce their direct recombination with electrons beside the ultrathin nanosheet effect in BM-PCN/Co-c. Fig. 3d shows time-resolved fluorescence spectra of the samples. Decay curves were well fitted to a tri-exponential model (S3) and the obtained results are shown in Fig. 3d. Three lifetimes ( $\tau_1$ – $\tau_3$ ) and their mean lifetime ( $\tau_m$ , 89.2 ns) of BM-PCN are all much longer than those of PCN ( $\tau_m$  = 17.9 ns), further suggesting the faster charge transfer from the inside to the surface of ultrathin nanosheets in BM-PCN, decreasing the direct charge recombination efficiency, but with subsequent surface radiative recombination.<sup>60</sup> Interestingly, the  $\tau_1$ – $\tau_3$  and  $\tau_m$  (10.8 ns) of BM-PCN/Co-c are much shorter than those of PCN, which should result from faster transfer of holes to  $E_d$  that effectively decreases the charge recombination efficiency, with subsequent nonradiative energy transformation.<sup>61</sup> The Co–OH doping effect also makes PCN/Co-c exhibit shorter  $\tau_1$ – $\tau_3$  and  $\tau_m$  (16.5 ns) than PCN. Fig. 3e shows the photocurrent response of the samples. Their anodic photocurrent density follows the order PCN < PCN/Co-c < BM-PCN < BM-PCN/Co-c, indicating gradually increased photogenerated charge separation efficiencies,<sup>62</sup> basically consistent with the PL results. The relatively high photocurrent response of BM-PCN benefits from the applied bias that effectively inhibits surface recombination of photogenerated charge carriers.

To assess charge mobility of the samples, their electrochemical impedance spectroscopy (EIS) spectra were tested with high-frequency data simply fitted to an equivalent circuit (Fig. S20†). The obtained charge transfer resistance ( $R_{ct}$ ) follows the order PCN (26  $\Omega$ ) > BM-PCN (18  $\Omega$ )  $\approx$  PCN/Co-c (19  $\Omega$ ) > BM-PCN/Co-c (13  $\Omega$ ). Apparently, BM-PCN/Co-c exhibits smaller  $R_{ct}$  than BM-PCN and PCN/Co-c, and PCN/Co-c exhibits smaller  $R_{ct}$  than PCN, indicating the highest charge transfer performance of BM-PCN/Co-c<sup>63</sup> which originates from the single-atom Co modification<sup>64</sup> that may increase the electron density to facilitate charge transport. The smaller  $R_{ct}$  of BM-PCN than that of PCN indicates the additional favorable effect of ultrathin nanosheets.<sup>65</sup> Fig. 3f shows electron paramagnetic resonance (EPR) spectra of the samples. All reveal one single Lorentzian

line centered at a  $g$  of 2.0039, attributed to unpaired electrons in heptazine rings.<sup>66</sup> In the dark, the EPR signal intensity follows the order PCN < BM-PCN < PCN/Co-c < BM-PCN/Co-c, and the stronger signal of BM-PCN than that of PCN results from formation of ultrathin nanosheets that enhances delocalization of unpaired electrons, while the stronger signal of BM-PCN/Co-c and PCN/Co-c mainly benefits from the Co doping that increases the delocalized electron density.<sup>67</sup> Under visible light irradiation, the samples exhibit remarkable signal enhancement, following the sequence PCN < BM-PCN < PCN/Co-c < BM-PCN/Co-c, similar to that of the signal intensity in the dark, suggesting that the increase in the delocalized electron density facilitates charge photoexcitation. The high delocalized electron density favors charge transport, consistent with the EIS results, and the high photoexcited charge density benefits enhancement of photocatalytic activity.

Photocatalytic OER activity of various samples was well evaluated using  $Ag^+$  as the sacrificial agent (Fig. S21†). The Co content in BM-PCN/Co-c was optimized according to the photocatalytic OER rates and BM-PCN-c exhibits no detectable OER activity (Fig. S22†), indicating indispensability of the Co–OH structure for the OER. The influence of the calcination temperature ( $T_c$ , °C) of BM-PCN/Co on OER rates of BM-PCN/Co-c ( $T_c$  = 460) and BM-PCN/Co-c $T_c$  was investigated and BM-PCN/Co-c exhibits the highest photoactivity (Fig. 4a), manifesting that the optimal calcination temperature is 460 °C. Under both simulated solar light and visible light irradiation ( $\lambda \geq 420$  nm), BM-PCN/Co-c exhibits substantially higher OER activity than PCN/Co-c (Fig. 4b), further suggesting the significance of the single-atom Co loading amount, and remarkably higher activity than common PCN/CoO<sub>x</sub> (with 0.75 wt% Co, obtained *via* photodeposition) and BM-PCN-c/Co(OH)<sub>2</sub> (with 0.75 wt% Co), demonstrating the high efficacy of the single-atom distribution of Co–OH in BM-PCN/Co-c. Besides, urea was used as the feedstock to synthesize carbon nitride (marked as PCN-urea) with a larger surface area (76 m<sup>2</sup> g<sup>−1</sup> (ref. 68)) than PCN, and PCN-urea was further used to synthesize PCN-urea/Co-c similar to the synthesis of BM-PCN/Co-c. The OER activity of BM-PCN/Co-c is prominently higher than that of PCN-urea/Co-c (with the optimized Co content and Co single atom distribution, Fig. S23†), suggesting the significant role of ball milling in fabricating the single-atom Co–N<sub>4</sub>OH structure. To quantitatively compare photoactivity of the samples, their mean OER rates under visible light illumination for 2 h are shown in Fig. 4c. The OER rate of BM-PCN/Co-c can reach  $\sim 37.3 \mu\text{mol h}^{-1}$ , about 13.8, 28.7, 2.6, and 2.0 times those of PCN/Co-c, PCN/CoO<sub>x</sub>, BM-PCN-c/Co(OH)<sub>2</sub>, and PCN-urea/Co-c, respectively. Comparatively, less N<sub>2</sub> was generated for BM-PCN/Co-c (Fig. S24†), further demonstrating the significance of single-atom Co–OH modification.

Photocatalytic oxygen evolution on BM-PCN/Co-c was also tested under monochromatic light irradiation (Fig. S25†). Apparently, BM-PCN/Co-c can exhibit OER activity even at a wavelength of 500 nm. The mean OER rate in 12 h decreases from 1.85 to 0.54  $\mu\text{mol h}^{-1}$  with increasing wavelengths from 400 to 500 nm (Fig. 4d), independent of light intensity of the Xe lamp and is mainly dependent on optical absorption capability



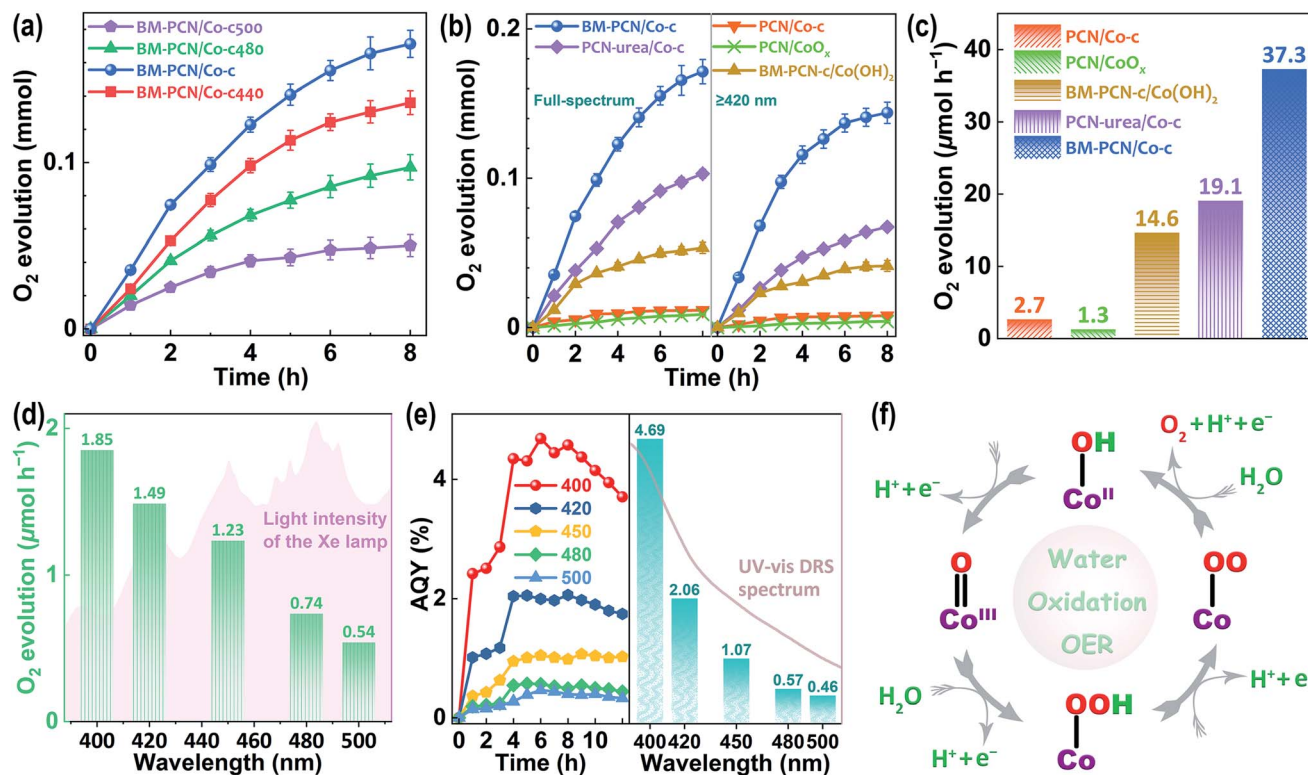


Fig. 4 (a) The influence of the calcination temperature ( $T_c$ , °C) of BM-PCN/Co on photocatalytic OER activity of BM-PCN/Co-c ( $T_c = 460$ ) and BM-PCN/Co-c- $T_c$ , under Xe-lamp illumination, with AgNO<sub>3</sub> as the sacrificial agent; (b) photocatalytic oxygen evolution on various samples under Xe-lamp illumination with or without using a 420-nm filter; (c) corresponding OER rates of the samples in 2 h; (d) photocatalytic OER rates of BM-PCN/Co-c under irradiation with various monochromatic light sources for 12 h; (e) apparent quantum yields (AQYs) of BM-PCN/Co-c at different wavelengths and reaction times and the highest AQY at every wavelength, along with the UV-DRS spectrum; and (f) proposed mechanism for photocatalytic water oxidation on the single-atom Co<sup>II</sup>-OH structure.

of BM-PCN/Co-c at various wavelengths (Fig. 3a). Fig. 4e shows apparent quantum yields (AQYs) of BM-PCN/Co-c at different reaction times and wavelengths. Basically, there are maxima of AQYs with increasing reaction time at every wavelength, suggesting the adverse effect of excessive photo-deposited Ag on surfaces of samples. These maxima are shown in Fig. 4e and accord well with the UV-vis DRS spectrum with increasing wavelengths. The maxima of AQYs at 400, 420, 450, and 500 nm can reach 4.69, 2.06, 1.07, and 0.46%, respectively. Compared with the reported photocatalytic OER results for PCN (Table S4†), BM-PCN/Co-c exhibits the top-class performance.

To investigate chemical stability of BM-PCN/Co-c, the cyclic OER experiment was conducted. After five consecutive runs, OER rates of BM-PCN/Co-c decrease less (Fig. S26a†), with the morphology similar to the original (Fig. S26b†). Co single atoms in the sample could still be distinctly observed by HAADF-STEM (Fig. S26c and d†). In addition, N 1s core-level XPS spectra of BM-PCN/Co-c are almost similar before and after the cyclic experiment (Fig. S26e†). These indicate the high stability of the basic framework structure of the sample. However, Co 2p core-level spectra show remarkable differences before and after the experiment, not only the Co<sup>II</sup> peak shift, probably owing to ion (e.g., IO<sub>4</sub><sup>-</sup>) adsorption, but also formation of a large amount of

Co<sup>III</sup> (Fig. S26f†). Coexistence of Co<sup>II</sup>/Co<sup>III</sup> may suggest the photocatalytic OER mechanism.

The proposed OER mechanism based on the Co-OH structure is shown in Fig. 4f, according to the reported results in Mn doped PCN.<sup>34</sup> Four holes are needed to complete four oxidation steps and obtain one O<sub>2</sub> molecule. The first step starting with one hole may involve formation of the Co<sup>III</sup>=O bond. The Co-N<sub>4</sub>OH structure should facilitate the water oxidation more compared with that of Co-N<sub>4</sub> without OH coordination, by leaving out the initial adsorption process of H<sub>2</sub>O molecules.<sup>34</sup> On the whole, the high photocatalytic OER activity of Co-PCN benefits from the Co-N<sub>4</sub>OH structure that not only effectively enhances optical absorption, and charge separation and transport, but also works as the highly active site for the OER.

## Conclusions

Single-atom Co<sup>II</sup>-OH modified PCN with an optimized Co content of 0.75 wt% (Co-PCN) was simply prepared *via* a ball milling-adsorption-calcination process and the Co content increases ~37 times thanks to the assistance of ball-milling that formed ultrathin nanosheets. The single-atom Co<sup>II</sup>-N<sub>4</sub>OH structure in Co-PCN was confirmed and evidenced to work as the active center for the OER. The Co<sup>II</sup>-OH modification was considered to endow Co-PCN with enhanced optical absorption,

and photogenerated charge separation and transport capability. Co-PCN exhibits a highly enhanced OER rate ( $\sim 37.3 \mu\text{mol h}^{-1}$  at the highest), compared with those of common PCN/ $\text{CoO}_x$  ( $\sim 28$  times lower) and the control sample prepared without ball milling ( $\sim 13$  times lower) under visible light irradiation, with the highest apparent quantum yields reaching 4.69, 2.06, 1.07, and 0.46% at 400, 420, 450, and 500 nm, respectively, and is among the best OER photocatalysts reported so far. This work provides an effective method to prepare efficient OER photocatalysts and may guide successive synthesis of high-performance photocatalysts (e.g., Z-scheme heterojunctions) for overall water splitting.

## Data availability

All experimental data are provided in the ESI.† Other data are available from the corresponding author upon reasonable request.

## Author contributions

F. Y. synthesized and characterized the samples and wrote this manuscript. Q. D., G. W. and Y. X. characterized the materials. H. L. conceived the experiments and revised the manuscript. W. H. revised the manuscript.

## Conflicts of interest

There are no conflicts to declare.

## Acknowledgements

This work was supported by the National Natural Science Foundation of China (No. 21872082) and the Young Scholars Program of Shandong University in China (No. 2018WLJH39). We are grateful for the assistance of Shandong University Structural Constituent and Physical Property Research Facilities (SDU SCPPRF) and Shiyanjia Lab (www.shiyanjia.com).

## Notes and references

- 1 D. Kirk-Davidoff, in *Green Chemistry*, ed. B. Török and T. Dransfield, Elsevier, Netherlands, 2018, p. 211.
- 2 H. Zhang, S. Zuo, M. Qiu, S. Wang, Y. Zhang, J. Zhang and X. W. Lou, *Sci. Adv.*, 2020, **6**, eabb9823.
- 3 J. Liu, Y. Li, X. Zhou, H. Jiang, H. G. Yang and C. Li, *J. Mater. Chem. A*, 2020, **8**, 17.
- 4 Y. Bai, K. Hippalgaonkar and R. S. Sprick, *J. Mater. Chem. A*, 2021, **9**, 16222.
- 5 S. Wang, Y. Wang, S.-Q. Zang and X. W. Lou, *Small Methods*, 2020, **4**, 1900586.
- 6 Z. Yi, J. Ye, N. Kikugawa, T. Kako, S. Ouyang, H. Stuart-Williams, H. Yang, J. Cao, W. Luo, Z. Li, Y. Liu and R. L. Withers, *Nat. Mater.*, 2010, **9**, 559.
- 7 G. Zhang, S. Zang, Z.-A. Lan, C. Huang, G. Li and X. Wang, *J. Mater. Chem. A*, 2015, **3**, 17946.
- 8 P. Li, X. Chen, H. He, X. Zhou, Y. Zhou and Z. Zou, *Adv. Mater.*, 2018, **30**, 1703119.
- 9 J. Yan, T. Wang, G. Wu, W. Dai, N. Guan, L. Li and J. Gong, *Adv. Mater.*, 2015, **27**, 1580.
- 10 G. He, W. Yang, W. Zheng, L. Gong, X. Wang, Y. An and M. Tian, *RSC Adv.*, 2019, **9**, 18222.
- 11 S. Lin, H. Huang, T. Ma and Y. Zhang, *Adv. Sci.*, 2020, **8**, 2002458.
- 12 X. Wang, K. Maeda, A. Thomas, K. Takanabe, G. Xin, J. M. Carlsson, K. Domen and M. Antonietti, *Nat. Mater.*, 2009, **8**, 76.
- 13 F. Fina, S. K. Callear, G. M. Carins and J. T. S. Irvine, *Chem. Mater.*, 2015, **27**, 2612.
- 14 Y. Wang, S. Z. F. Phua, G. Dong, X. Liu, B. He, Q. Zhai, Y. Li, C. Zheng, H. Quan, Z. Li and Y. Zhao, *Chem*, 2019, **5**, 2775.
- 15 W. J. Ong, L. L. Tan, Y. H. Ng, S. T. Yong and S. P. Chai, *Chem. Rev.*, 2016, **116**, 7159.
- 16 Z. Liang, X. Zhuang, Z. Tang, H. Li, L. Liu and W. Kang, *J. Mater. Chem. A*, 2021, **9**, 6805.
- 17 Q. Han, Z. Cheng, B. Wang, H. Zhang and L. Qu, *ACS Nano*, 2018, **12**, 5221.
- 18 S. Yu, J. Li, Y. Zhang, M. Li, F. Dong, T. Zhang and H. Huang, *Nano Energy*, 2018, **50**, 383.
- 19 G. Liu, H. Lv, Y. Zeng, M. Yuan, Q. Meng, Y. Wang and C. Wang, *Trans. Tianjin Univ.*, 2021, **27**, 139.
- 20 P. Zhou, Y. Chao, F. Lv, J. Lai, K. Wang and S. Guo, *Sci. Bull.*, 2020, **65**, 720.
- 21 P. Yang, H. Ou, Y. Fang and X. Wang, *Angew. Chem., Int. Ed.*, 2017, **56**, 3992.
- 22 J. Fu, J. Yu, C. Jiang and B. Cheng, *Adv. Energy Mater.*, 2018, **8**, 1701503.
- 23 C. Han, L. Du, M. Konarova, D.-C. Qi, D. L. Phillips and J. Xu, *ACS Catal.*, 2020, **10**, 9227.
- 24 G. Zhang, Z. A. Lan and X. Wang, *Chem. Sci.*, 2017, **8**, 5261.
- 25 X. Chen, R. Shi, Q. Chen, Z. Zhang, W. Jiang, Y. Zhu and T. Zhang, *Nano Energy*, 2019, **59**, 644.
- 26 Z. Pan, Y. Zheng, F. Guo, P. Niu and X. Wang, *ChemSusChem*, 2017, **10**, 87.
- 27 L. Ge, C. Han, X. Xiao and L. Guo, *Appl. Catal., B*, 2013, **142–143**, 414.
- 28 F. Raziq, L. Sun, Y. Wang, X. Zhang, M. Humayun, S. Ali, L. Bai, Y. Qu, H. Yu and L. Jing, *Adv. Energy Mater.*, 2018, **8**, 1701580.
- 29 T. Kanazawa, K. Kato, R. Yamaguchi, T. Uchiyama, D. Lu, S. Nozawa, A. Yamakata, Y. Uchimoto and K. Maeda, *ACS Catal.*, 2020, **10**, 4960.
- 30 G. Zhang, S. Zang and X. Wang, *ACS Catal.*, 2015, **5**, 941.
- 31 J. Liu, Y. Liu, N. Liu, Y. Han, X. Zhang, H. Huang, Y. Lifshitz, S.-T. Lee, J. Zhong and Z. Kang, *Science*, 2015, **347**, 970.
- 32 W. Che, W. Cheng, T. Yao, F. Tang, W. Liu, H. Su, Y. Huang, Q. Liu, J. Liu, F. Hu, Z. Pan, Z. Sun and S. Wei, *J. Am. Chem. Soc.*, 2017, **139**, 3021.
- 33 K. Zhang, L. Wang, X. Sheng, M. Ma, M. S. Jung, W. Kim, H. Lee and J. H. Park, *Adv. Energy Mater.*, 2016, **6**, 1502352.
- 34 S. Sun, G. Shen, J. Jiang, W. Mi, X. Liu, L. Pan, X. Zhang and J. J. Zou, *Adv. Energy Mater.*, 2019, **9**, 1901505.





- 35 W. Liu, L. Cao, W. Cheng, Y. Cao, X. Liu, W. Zhang, X. Mou, L. Jin, X. Zheng, W. Che, Q. Liu, T. Yao and S. Wei, *Angew. Chem., Int. Ed.*, 2017, **56**, 9312.
- 36 D. Zhao, C. L. Dong, B. Wang, C. Chen, Y. C. Huang, Z. Diao, S. Li, L. Guo and S. Shen, *Adv. Mater.*, 2019, **31**, e1903545.
- 37 D. Zhao, Y. Wang, C.-L. Dong, Y.-C. Huang, J. Chen, F. Xue, S. Shen and L. Guo, *Nat. Energy*, 2021, **6**, 388.
- 38 Y. Li, Y. Wang, C. L. Dong, Y. C. Huang, J. Chen, Z. Zhang, F. Meng, Q. Zhang, Y. Huangfu, D. Zhao, L. Gu and S. Shen, *Chem. Sci.*, 2021, **12**, 3633.
- 39 S.-M. Xu, T. Pan, Y.-B. Dou, H. Yan, S.-T. Zhang, F.-Y. Ning, W.-Y. Shi and M. Wei, *J. Phys. Chem. C*, 2015, **119**, 18823.
- 40 J. Yan, H. Wu, H. Chen, L. Pang, Y. Zhang, R. Jiang, L. Li and S. Liu, *Appl. Catal., B*, 2016, **194**, 74.
- 41 H. Schreyer, R. Eckert, S. Immohr, J. de Bellis, M. Felderhoff and F. Schüth, *Angew. Chem., Int. Ed.*, 2019, **58**, 11262.
- 42 D. Deng, X. Chen, L. Yu, X. Wu, Q. Liu, Y. Liu, H. Yang, H. Tian, Y. Hu, P. Du, R. Si, J. Wang, X. Cui, H. Li, J. Xiao, T. Xu, J. Deng, F. Yang, P. N. Duchesne, P. Zhang, J. Zhou, L. Sun, J. Li, X. Pan and X. Bao, *Sci. Adv.*, 2015, **1**, e1500462.
- 43 S. Maleki and A. Karimi-Jashni, *Appl. Clay Sci.*, 2017, **137**, 213.
- 44 Q. Han, F. Zhao, C. Hu, L. Lv, Z. Zhang, N. Chen and L. Qu, *Nano Res.*, 2015, **8**, 1718.
- 45 Z. Guo, Y. Xie, J. Xiao, Z. J. Zhao, Y. Wang, Z. Xu, Y. Zhang, L. Yin, H. Cao and J. Gong, *J. Am. Chem. Soc.*, 2019, **141**, 12005.
- 46 L. Qian and Y. Miao, *Polyhedron*, 2019, **160**, 213.
- 47 T.-Q. Zi, X.-R. Zhao, C. Liu, Y.-Q. Cao and A.-D. Li, *J. Alloys Compd.*, 2021, **855**, 157446.
- 48 J.-K. Chang, C.-M. Wu and I. W. Sun, *J. Mater. Chem.*, 2010, **20**, 3729.
- 49 J. Xu, L. W. Zhang, R. Shi and Y. F. Zhu, *J. Mater. Chem. A*, 2013, **1**, 14766.
- 50 Q. Deng, G. Ba, T. Huo, H. Li, G. Wang, F. Yu and W. Hou, *Appl. Surf. Sci.*, 2020, 148427.
- 51 Z. Liang, Y. Xia, G. Ba, H. Li, Q. Deng and W. Hou, *J. Mater. Chem. A*, 2019, **7**, 25824.
- 52 J. Wu, X. Ji, X. Yuan, Z. Zhao, Y. Li, B. Wen, H. Zhang, D. Yu, Y. Zhao and Y. Tian, *Chem. Mater.*, 2019, **31**, 9188.
- 53 A. B. Jorge, D. J. Martin, M. T. S. Dhanoa, A. S. Rahman, N. Makwana, J. Tang, A. Sella, F. Corà, S. Firth, J. A. Darr and P. F. McMillan, *J. Phys. Chem. C*, 2013, **117**, 7178.
- 54 J. Ran, T. Y. Ma, G. Gao, X.-W. Du and S. Z. Qiao, *Energy Environ. Sci.*, 2015, **8**, 3708.
- 55 W. Zhang, Q. Peng, L. Shi, Q. Yao, X. Wang, A. Yu, Z. Chen and Y. Fu, *Small*, 2019, **15**, 1905166.
- 56 C. Zhu, L. Meng, J. Zhang, S. Qin, W. Lai, B. Qiu, J. Yuan, Y. Wan, W. Huang and Y. Li, *Adv. Mater.*, 2021, **33**, 2100474.
- 57 X. Li, P. Cui, W. Zhong, J. Li, X. Wang, Z. Wang and J. Jiang, *Chem. Commun.*, 2016, **52**, 13233.
- 58 K. Watanabe, A. Iwase, S. Nozawa, S.-i. Adachi and A. Kudo, *ACS Sustainable Chem. Eng.*, 2019, **7**, 9881.
- 59 K. Omika, K. Takahashi, A. Yasui, T. Ohkouchi, H. Osawa, T. Kouchi, Y. Tateno, M. Suemitsu and H. Fukidome, *Appl. Phys. Lett.*, 2020, **117**, 171605.
- 60 L. Cavigli, F. Bogani, A. Vinattieri, V. Faso and G. Baldi, *J. Appl. Phys.*, 2009, **106**, 053516.
- 61 T. Huo, G. Ba, Q. Deng, F. Yu, G. Wang, H. Li and W. Hou, *Appl. Catal., B*, 2021, **287**, 119995.
- 62 P. Zhang, X. F. Lu, D. Luan and X. W. Lou, *Angew. Chem., Int. Ed.*, 2020, **59**, 8128.
- 63 X. Zhang and G. Lu, *Carbon*, 2016, **108**, 215.
- 64 X. Xiong, C. Mao, Z. Yang, Q. Zhang, G. I. N. Waterhouse, L. Gu and T. Zhang, *Adv. Energy Mater.*, 2020, **10**, 2002928.
- 65 L. Zhou, J. Feng, B. Qiu, Y. Zhou, J. Lei, M. Xing, L. Wang, Y. Zhou, Y. Liu and J. Zhang, *Appl. Catal., B*, 2020, **267**, 118396.
- 66 G. Dong, W. Ho and C. Wang, *J. Mater. Chem. A*, 2015, **3**, 23435.
- 67 S. Li, S. Zhao, X. Lu, M. Ceccato, X.-M. Hu, A. Roldan, J. Catalano, M. Liu, T. Skrydstrup and K. Daasbjerg, *Angew. Chem., Int. Ed.*, 2021, **60**, 22826.
- 68 F. Yang, G. Ba, Z. Wang and H. Li, *J. Colloid Interface Sci.*, 2021, **594**, 64.

